Coastal infrastructure operativity against flooding – a methodology

Cristobal Rodriguez-Delgado[a,b], Rafael J. Bergillos[c,*], Gregorio Iglesias[d,a]

[a]*School of Engineering, University of Plymouth, Plymouth PL4 8AA, UK*
[b]*PROES Consultores, Calle San Germán 39, 28020 Madrid, Spain*
[c]*Hydraulic Engineering Area, Department of Agronomy, University of Cordoba, Rabanales Campus, Leonardo da Vinci Building, 14071 Córdoba, Spain*
[d]*MaREI, Environmental Research Institute & School of Engineering, University College Cork, College Road, Cork, Ireland*

Abstract

The operativity of the transport infrastructures and urban developments protected by coastal structures is conditioned by flooding events and the resulting wave overtopping. This work presents a methodology to assess the operational conditions of infrastructures located in coastal areas based on the combination of advanced statistical techniques, laboratory experiments and state-of-the-art numerical models properly validated. It is applied to a case study in the SW coast of England, the railway seawall at Dawlish, which was subjected to recurrent wave overtopping until its dramatic collapse in February 2014. To quantify the increase in overtopping discharges with wave height and water level, we define an *ad hoc* variable, the *effective overtopping forcing*, which explains 98% of the variability of the overtopping discharge. The return periods associated to the operational thresholds for coastal structures protecting people and railways are also obtained. The proposed methodology enables the assessment of the overtopping discharge induced by a given sea state and, thus, check if a coastal infrastructure will be or not operational under any expected marine condition. This innovative methodology can also be used to analyse the flooding event consequences on urban areas protected by coastal infrastructures.

*Corresponding author.
E-mail address: rafael.bergillos@uco.es

Keywords: Coastal flooding; Seawall; Operationality; Statistics; Laboratory experiments; Numerical modelling

1. Introduction

Coastal flooding is one of the environmental hazards with the greatest potential impact on human activity [1–6]. Flooding typically occur as a result of wave overtopping of coastal structures [7–9]. These flooding events will be more frequent and severe in the next decades due the rise in sea level and other consequences of climate change [10–15]. When coastal structures protect transport infrastructure (railway lines, roads, etc.), wave overtopping can disrupt the chain of transport, with strong repercussions for the society and economy of the region. Some recent studies have dealt with the impacts of wave overtopping on transport infrastructure (e.g., [16] or [17]). Wave overtopping has also been studied in connection with flood-control structures [18–22], rockfill dams [23, 24] and coastal structures [25, 26].

Coastal structures are designed to fulfil specific social, economic and/or environmental functions. They often have a multi-functional nature [27]. In the case of seawalls, their primary function is to protect urban areas and transport infrastructure against coastal flooding [28–36]. The operativity of seawalls is mainly conditioned by wave overtopping. Thus, it is essential to predict overtopping discharges accurately [37–40].

The design conditions for a coastal structure are commonly obtained through extreme value analysis of long-term data series, in which the design significant wave height is calculated for a prescribed return period. In the case of wave overtopping, there is another factor of utmost importance: the water level, which is determined by the astronomical tide and storm surge. On top of that, the rise in sea level will have an important impact on return periods, giving even more importance to the water level at the toe of the coastal structures. Multivariate extreme value analysis must be applied, therefore, to establish the joint probability distribution of water level and wave height [41–43].

Wave overtopping has been traditionally assessed by means of physical modelling. Laboratory experiments have provided valuable data [44–51]. Based on these data, design equations have been derived [52–54] and neural network techniques have been applied [55–58]. However, structures with non-standard geometries require *ad hoc* tests [59]. As this may not always be possible for reasons of cost and time, especially in order to assess the operativity of an existing structure, numerical modelling of wave overtopping is becoming ever more popular. Several numerical models have been developed so far to determine overtopping rates on coastal structures [60–63]. Among them, CFD (Computational Fluid Dynamics) models, based on the RANS (Reynolds-Averaged Navier-Stokes) equations and the VOF (Volume-of-Fluid) method [64] for capturing the free surface, are able to simulate the non-linearities in wave-structure interaction, which renders them particularly attractive.

There is very little knowledge concerning the effects of wave overtopping on transport systems in the lee of seawalls or breakwaters. [65] studied the effects of wave overtopping jets on pedestrians and vehicles based on physical modelling and suggested some guidelines for operational purposes. More recently, these guidelines have been updated in [66], including operational thresholds for railways, highways, roads and people.

In this paper, a novel methodology to assess the operational conditions of infrastructures against coastal flooding is proposed. It is based on the combination of multivariate extreme analysis and numerical modelling applications (Section 2). The methodology is applied to a study case: the Dawlish seawall, in the UK (Section 3). This infrastructure is infamous for its failure during the storms of February 2014 and the consequent disruption to the all-important railway line connecting SW England with the rest of the country.

2. Description of the methodology

The methodology proposed in this work to quantify the operational conditions is summarized in Fig. 1. Based on the deep-water water level (η) and significant wave height (H_{s0}) data at a given study area, an extreme value analysis for both variables is first required to obtain the joint probability distribution (Section 2.1). To characterize the whole universe of water level and significant wave height combinations, a mesh is created based on the selection of N pairs of values (η, H_{s0}). The sea states selected are propagated from deep water to the location of the structure using a numerical wave propagation model (Section 2.2). The local wave conditions thus obtained are employed as input conditions to apply a CFD model (Section 2.3), which allows computing wave overtopping discharges. Based on these overtopping discharge values, the operational conditions of the infrastructure against coastal flooding are assessed (Section 2.4).

2.1. Assessment of extreme values and joint probability

In order to assess the risks associated with wave overtopping, it is crucial to determine the joint probability of extreme water levels and wave heights. In this work, the novel statistical dependence methodology for compound events developed by the Joint Research Centre of the European Commission [67] is used.

For any combination of water level and significant wave height, the joint return period of occurrence is defined as

$$T_{X,Y} = \sqrt{\frac{T_x \cdot T_y}{\chi^2}}, \tag{1}$$

where T_x and T_y are the return periods of the water level and significant wave height, respectively. The parameter χ is the dependence measure, calculated as

$$\chi\left(u\right) = 2 - \frac{\ln P\left(U \leq u, V \leq u\right)}{\ln P\left(U \leq u\right)}, \tag{2}$$

where u is a common threshold selected as the 99th percentile of the significant wave height from the wave dataset and of the water level from the water level record. This dependence coefficient varies between 0 (no correlation) and 1 (total correlation).

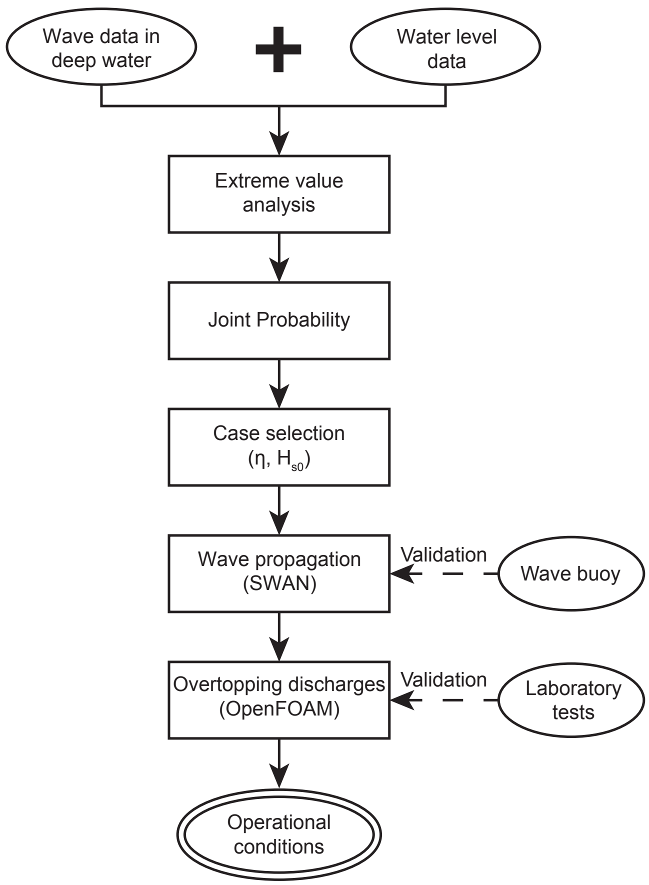

Figure 1: Flow chart of the methodology proposed in this work.

2.2. Numerical modelling of wave propagation

The sea states in deep water are propagated toward the location of the outer boundary of the CFD model by means of SWAN, a 3rd generation spectral wave model [68, 69]. This model reproduces the main processes related to wave propagation, such as refraction, shoaling, breaking as well as diffraction, transmission and reflection induced by obstacles. The SWAN model has been used over the past few years for a wide range of coastal engineering applications [70–86].

2.3. Numerical modelling of wave overtopping discharge

In order to obtain the wave overtopping discharge for each one of the N combinations (η, H_{s0}) selected and propagated with SWAN, the use of a CFD numerical model is required. OpenFOAM® [87] was chosen due to its open-source character along with its wide and active community of users.

2.4. Assessment of operational conditions

The operational conditions of a coastal infrastructure are defined by its functionality. In the case of seawalls, the main goal of the structure is generally to protect the transport infrastructures and people in the lee of the seawalls. Eurotop [66] defines some limitations to overtopping discharges in terms of structural design and, more specifically for structures protecting transport infrastructures and people.

3. Application of the methodology to a case study

3.1. Description of the study site

The study site, Dawlish, is located in the Lyme Bay (SW England, UK), in the western margin of the English Channel (Fig. 2). The Dawlish seawall protects the railway line from London to Penzance, which was opened to the traffic in 1846 and designed by I.K. Brunel. This line is the only rail connection between the SW of England and the rest of the country. The section of the line between Teignmouth and Dawlish, which connects the cities of Plymouth and Exeter, follows the shoreline and is protected from wave action by a nearly vertical seawall (the aforementioned Dawlish seawall). This section has suffered multiple disruptions throughout its history due to wave overtopping [88].

The storm of February 2014 is a good example of the havoc that can be wreaked by natural hazards on transport infrastructure. Part of the seawall collapsed under the combination of extreme waves and water levels, leaving the rails dangling in the air (Fig. 3). The line stayed close to the traffic over months, with serious repercussions for the region. The cross-section of the seawall varies along Dawlish. To apply the methodology proposed in this paper, the section corresponding to Riviera Terrace was considered (Fig. 4). This was the zone that suffered most of the damage during the storm event in February 2014 (Fig. 3).

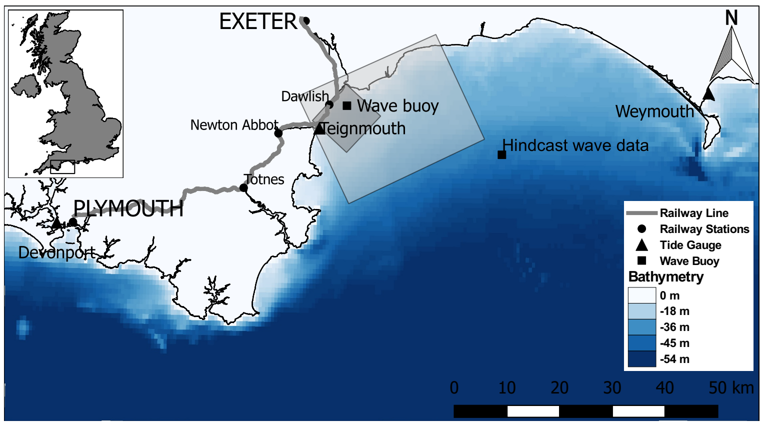

Figure 2: Location of the study area (top-left panel). The central panel shows the track of the railway line and the more important stations connected, along with the location of the tide gauges, wave buoy and hindcast data point, the grids employed in the propagation model and the bathymetry.

Figure 3: Seawall collapsed at Dawlish on 6 February 2014, with rails hanging in mid-air. Source: http://www.geograph.org.uk/photo/3838795. Copyright: Derek Harper, Creative Commons Licence.

The wave regime at the study area is characterised by the joint influence of North Atlantic swells with SW mean direction and locally generated waves. The 50%, 90% and 99% non-exceed deep-water significant wave heights are 0.9 m, 2.1 m and 3.5 m, respectively. The maximum observed value of significant wave height is 10.4 m, corresponding to the storm of February 2014. The tidal range at Teignmouth is 4.9 m.

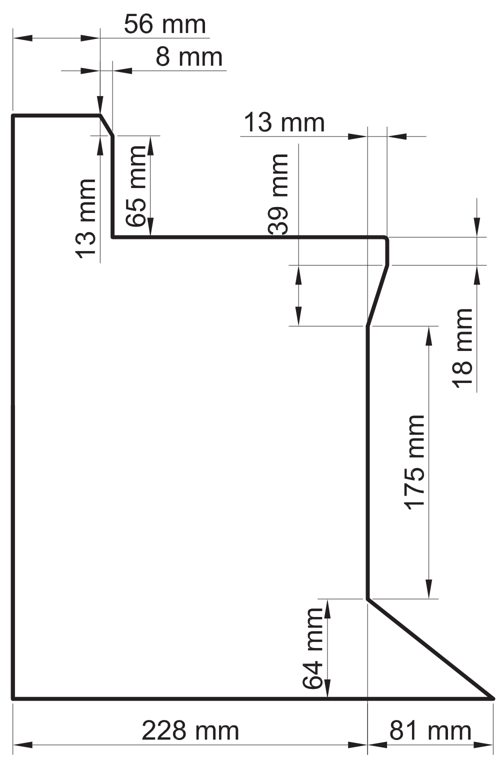

Figure 4: Cross-section of the Dawlish seawall at a 1:20 scale.

3.2. Extreme values

The wave data used in this work were obtained through the WAM North Atlantic hindcast wave model (Fig. 2). This dataset contains a 50-year time series of hourly wave hindcast data including significant wave heights, spectral peak periods, and mean incoming wave directions. Based on these data, return periods for extreme wave height values were assessed using the r-largest method [89]. The five maximum wave height values per annum were selected over the 50-year time series, and a EV (Generalised Extreme Value) distribution was fitted.

The tide gauge nearest to Dawlish is situated at Teignmouth, 6 km away. Its record only comprises 6 years of data, an insufficient length to assess return periods properly. To extend the record, the Inverse Distance Weighting (IDW) method was applied using the tide gauges at Devonport and Weymouth (Fig. 2). The distance coefficients for the IDW method were calibrated and validated using the data of the Teignmouth record, and a correlation coefficient $R = 0.99$ was obtained. In this way, the record was extended to 26 years. Likewise, the r-largest method was employed to obtain the return periods associated to extreme water levels, using again the five annual maxima per year and the GEV distribution.

The diagnostic plots of the GEV distribution fitted to the five maximum values per year of significant wave height are shown in Fig. 5. The GEV is defined by three parameters: scale (σ), shape (k) and location (μ). The value of k characterizes the tail behaviour of the function and divides the GEV distribution into three subtypes: Type I ($k = 0$), Type II ($k > 0$) and Type III ($k < 0$). The best fit was obtained with $k = 0.0518$ (Fig. 5c). This results in a Type II GEV function, with positive first and second derivatives (Fig. 5c), implying that H_s increases with the return period indefinitely. The divergence of the tail of the distribution accounts for the probability of heavy storms, such as the infamous February 2014 gale, which resulted in extreme wave overtopping and the subsequent collapse of the Dawlish seawall.

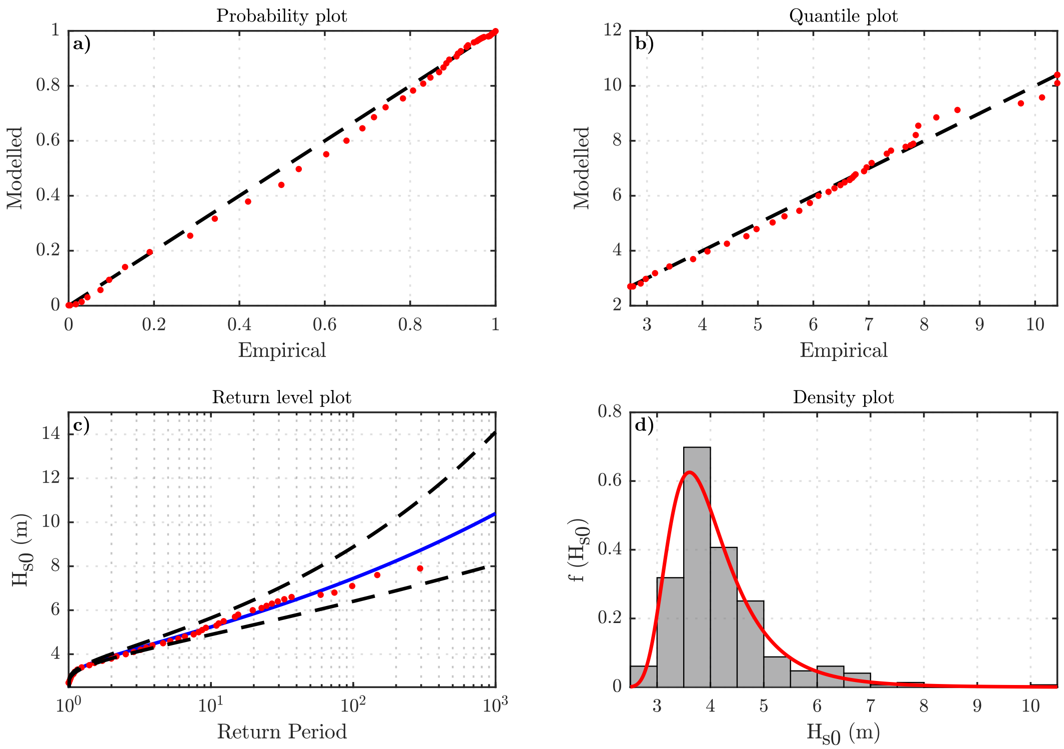

Figure 5: Diagnostics plots for the GEV distribution fitted to the significant wave heights in deep water (H_{s0}).

On the other hand, the diagnostic plots of the GEV distribution fitted to the water level data at Teignmouth (Fig. 6) have an optimum shape parameter equal to $k = -0.13$. This results in a Type III GEV distribution and a different tail behaviour, with a negative second derivative that hints at an asymptotic tendency for large values of the return period (Fig. 6c). The water level is controlled by the astronomical tide and the meteorological influences which govern the storm surge (atmospheric pressure and wind). The astronomical tide is a deterministic nature and the influence of storm surge can only go so far. For this reason, the tail behaviour of the GEV distribution is clearly different in the case of water level.

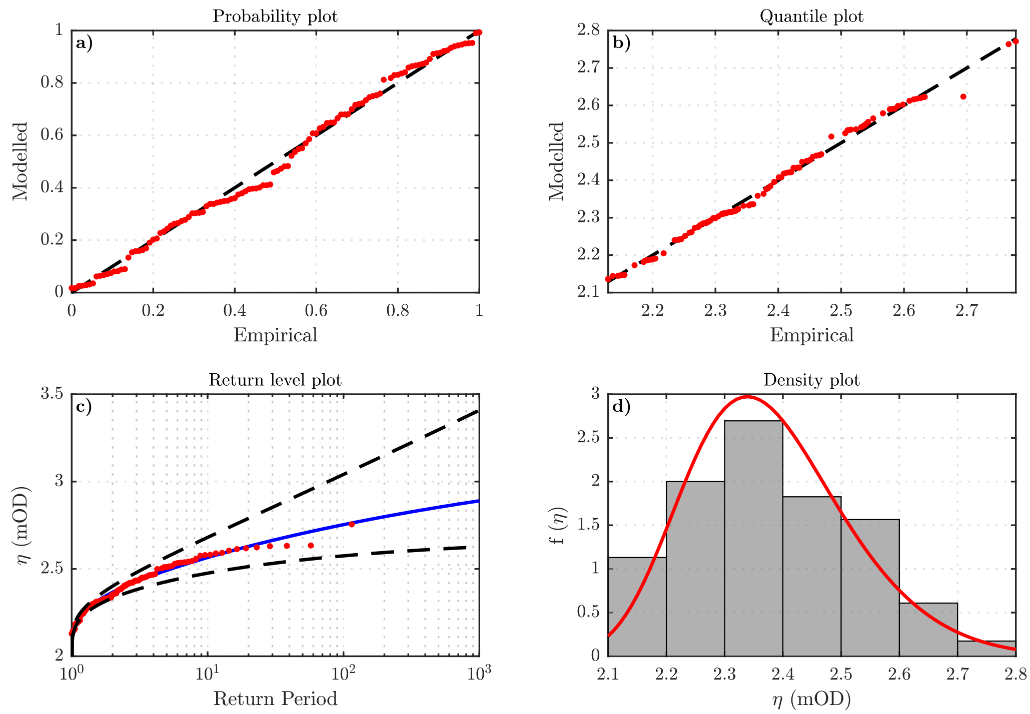

Figure 6: Diagnostics plots for the GEV distribution fitted to the water levels (η).

3.3. *Joint probability*

The joint probability analysis yields a dependence coefficient $\chi = 0.57$, which implies a strong correlation between extreme water levels and wave heights. The outputs of the analysis are the joint probability curves for joint return period values of 5, 10, 25, 50, 100, 250 and 500 years, i.e. the isolines of joint return period in the (η, H_{s0}) plane (Fig. 7). In this way, the area between the isoline, the x-axis and the y-axis may be assumed as a measurement of the number of pairs (η, H_{s0}) whose joint return period is equal or lower than the value of the isoline.

Therefore, a comparison between the area under the isoline of joint return period (calculated considering the water level and significant wave height as independent variables) and that obtained using the dependence coefficient, leads to an estimation of the number of cases whose probability of occurrence would be underrated with traditional independent analysis. The cases with a longer joint return period are the most underestimated. The areas under the 500-year, 250-year and 100-year isolines increase by 29.7%, 26.7% and 22.5%, respectively; whereas the increase in the area under the 5-year isoline is equal to 6.2%.

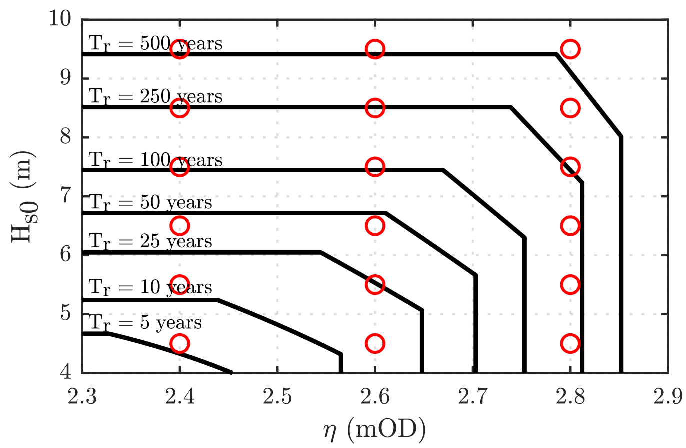

Figure 7: Isolines corresponding to return period values of 5, 10, 25, 50, 100, 250 and 500 years (black lines), and pairs (η,H_{s0}) analysed (red dots).

3.4. Wave propagation

The computational domain used to perform the wave propagation with SWAN is divided into two grids (Fig. 2): (i) a coarse grid composed by 207×207 rectangular cells of 130×105 m, covering the region between 40 m water depths and the coastline; and (ii) a nested grid composed by 406×406 rectangular cells of 23×22 m, covering the shallow water area, with maximum depths of 23 m. The bathymetry was obtained from the UKHO INSPIRE portal. The frequency space, between 0.03 and 0.4 Hz, was divided into 32 bins, while the directional space covered 360° with a resolution of 5° (72 directional bins).

The SWAN model was calibrated and validated using data from the coastal wave buoy located at Dawlish (Fig. 2), managed by the Channel Coastal Observatory. The length of this dataset is 6 years of hourly wave data, including significant wave height, spectral peak period, and mean incoming wave direction. The calibration period, from 1 February 2014 to 28 February 2014, was chosen for its extreme wave conditions. The SWAN model was forced using the WAM data and taking into account the following processes: bottom friction, non-linear triad interactions, refraction, diffraction, whitecapping and depth-induced wave breaking. The results of the validation are depicted in Fig. 8. The correlation coefficient between the results of the model and the wave buoy observations is $R = 0.94$, with a RMSE= 0.25 m.

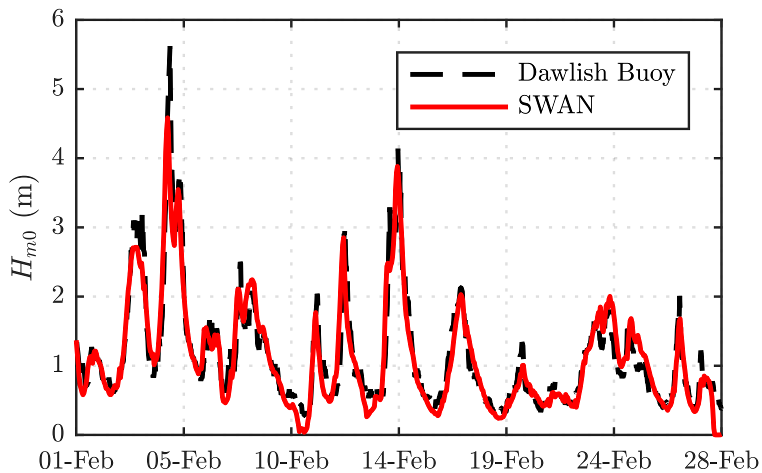

Figure 8: Comparison between measured and modelled significant wave height time series in February 2014 at the location of the wave buoy (Fig. 2).

3.5. Wave overtopping

3.5.1. Laboratory experiments

The physical model of the seawall was built in marine plywood at a 1:20 scale (Fig. 4). The tests were carried out in the COAST laboratory at the University of Plymouth, in a 0.6-m-wide and 35-m-long wave flume (Fig. 9). The wave paddle is equipped with an active wave absorption control system. The toe of the model was situated at a distance of 23.88 m from the paddle. In front of the model, a ramp was located to reproduce the bathymetry; whereas the still water level was set at 0.5 m. Eight resistive wave gauges were used during the experiments (Fig. 9). Seven wave gauges (WG1–WG7) were placed between the wave paddle and the model, and an additional wave gauge (WG8) was located behind the model to measure the overtopping volume.

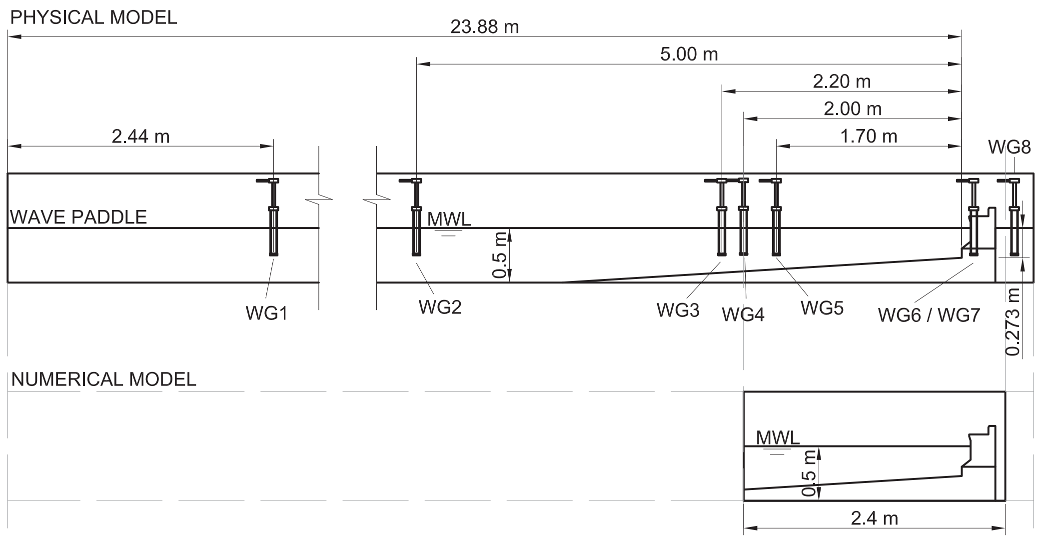

Figure 9: Physical and numerical set-ups.

Eighteen irregular wave tests were carried out, covering significant wave height valuess between 1.7 m and 4.4 m, and peak period values varying from 7 s to 13 s (prototype scale). The incident and reflected wave spectra were separated through a least-squares method using the measurements of three wave gauges (WG 3, WG 4 and WG 5). These data were employed to validate the CFD model (Section 3.5.2).

3.5.2. Set-up and validation of OpenFOAM®

The computational domain spans a total length of 2.4 m, between the position of WG4 and the rear of the model (Fig. 9). Thus, the computational cost was reduced without compromising the accuracy of the simulations. The incident wave spectra at the upstream boundary (WG4) were obtained by means of the aforementioned incident-reflected wave analysis. The height of the computational domain was 1.2 m and, as there is no directionality in the irregular waves generated, the width of the computational domain was covered by a cell.

The initial meshing of the computational domain was generated by the "blockMesh" utility included in OpenFOAM®, and it was composed by rectangular cells of 1 x 0.5 cm. To simulate the interaction between flow and model, the ramp and the seawall were removed from the mesh using the utility "snappyHexMesh", also included in OpenFOAM® (Fig. 10). The desired still water level was achieved setting $\alpha = 1$ (full of water) for those cells with $z \leq \eta$ and $\alpha = 0$ (full of air) for $z > \eta$, where η is the desired water level for each test.

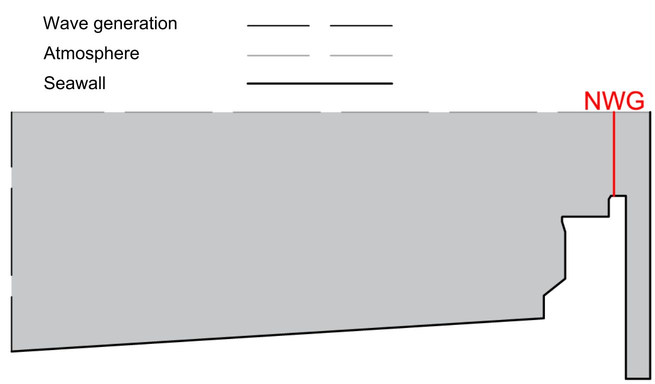

Figure 10: Computational domain, boundary conditions and numerical wave gauge (NWG) used in OpenFOAM®.

The numerical tests for the validation were carried out considering the same wave conditions as the physical model experiments (Table 1), and with the same number of waves (200). Velocities and elevations of the free surface over the freeboard were determined by means of a numerical wave gauge. The correlation coefficient obtained was $R = 0.89$ (Fig. 11), presenting a greater statistical correlation for overtopping discharges below 50×10^{-3} l/s per m.

Table 1: Overtopping discharges measured in the laboratory and obtained with the numerical model [H_s: significant wave height; T_p: spectral peak period; Q_m: mean overtopping discharge measured in the laboratory; Q_n: mean overtopping discharge obtained with the numerical model].

H_s (m)	T_p (s)	Q_m (10^{-3} l/s per m)	Q_n (10^{-3} l/s per m)
0.085	2.01	0	0
0.085	2.45	1.4	0.4
0.085	2.9	0	0
0.112	1.56	1	4
0.112	2.01	3	11
0.112	2.45	14	12.7
0.112	2.9	23	13
0.14	1.56	7.4	4.1
0.14	2.01	36	69
0.14	2.45	70	109
0.14	2.9	125	100
0.166	1.56	22	24
0.166	2.01	54	52
0.166	2.45	163	203
0.166	2.9	248	179
0.194	2.01	179	83
0.194	1.56	27	16
0.221	1.56	42	28

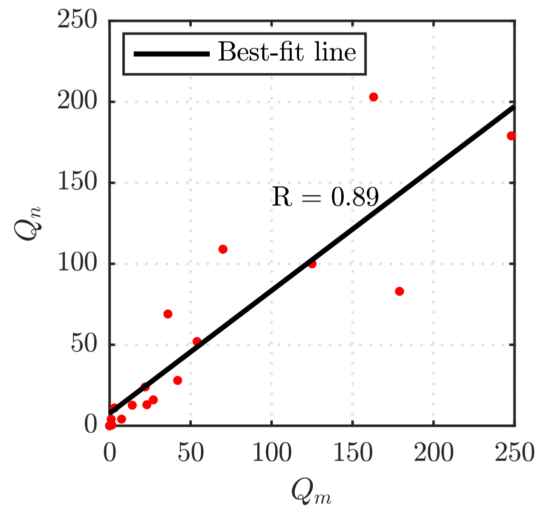

Figure 11: Scatter diagram of the mean overtopping discharges measured in the laboratory experiments (Q_m) and modelled with the CFD numerical model (Q_n). R is the correlation coefficient.

3.5.3. Wave overtopping discharges

Apart from water level and significant wave height, for the definition of a sea state, the spectral peak period (T_p) is required. As the objective of this work is to characterize the operational conditions of a coastal structure against extreme events (floodings), only sea states with $H_{s0} > 3$ m were considered, referred to henceforth as extreme sea states. The universe of extreme sea states in the hindcast dataset was divided into three regions based on wave steepness, H_{s0}/L_0, where L_0 is the wavelength in deep water, which is related to the peak period as follows:

- Region I: high-steepness sea states, with $0.025 < H_{s0}/L_0$,
- Region II: mid-steepness sea states, with $0.020 < H_{s0}/L_0 < 0.025$, and
- Region III: low-steepness sea states, with $H_{s0}/L_0 < 0.020$.

Curves were fitted to the data in each region, defined by:

$$T_p = 3.40 H_{s0}^{0.58} + 1.34, \tag{3}$$

$$T_p = 6.87 H_{s0}^{0.44} - 1.67, \text{ and} \tag{4}$$

$$T_p = 2.63 H_{s0}^{0.74} + 6.53. \tag{5}$$

Equations 3, 4 and 5 correspond to the best-fit curves of Regions I, II and III, respectively. Regions I and II show a strong correlation between H_{s0} and T_p, with $R = 0.76$ and $R = 0.92$, respectively. By contrast, Region III shows a weaker correlation, with $R = 0.38$. In any case, Regions I and II are the most interesting from the standpoint of the operativity of the seawall, since they contain the most extreme wave heights. The majority of extreme sea states come from the SW; however, these sea states can have different provenances: ocean swells propagating into the Channel or locally-generated wind waves, the latter with comparatively higher wave steepness. The division of the universe of significant wave heights and peak periods into two regions (I and II) seeks to represent these two provenances.

Eighteen pairs (η, H_{s0}) were defined by creating a mesh around the isolines of joint return period (Fig. 7). For each of these pairs defined, two values of the peak wave period were determined using Eqs. 3 and 4. This provided a total of 36 cases for the combined numerical modelling approach (wave propagation and CFD). The results obtained with the combined numerical modelling are presented in Table 2. For ten of the pairs (η, H_{s0}) tested, the discharge is greater in Region II (mid-steepness) than in Region I (high-steepness). Five pairs exhibit the opposite behaviour, and in the rest of cases there is no overtopping. Independently of the wave steepness region considered, the mean overtopping discharge increases with increasing water levels and significant wave heights (Fig. 12a, b). The averages of the mean overtopping discharges for constant values of η and H_{s0} are shown in Table 3.

Table 2: Results of the combined numerical models [η: water level; H_{s0}: significant wave height in deep water; T_{pI}: peak period in region I; Q_{nI}: mean overtopping discharge in Region I; T_{pII}: peak period in region II; Q_{nII}: mean overtopping discharge in Region II].

Case Id.	η (mOD)	H_{s0} (m)	T_{pI} (s)	Q_{nI} (ls^{-1}m^{-1})	Case Id.	η (mOD)	H_{s0} (m)	T_{pII} (s)	Q_{nII} (ls^{-1}m^{-1})
1_{I}	2.4	4.5	9.5	0	1_{II}	2.4	4.5	11.6	0
2_{I}	2.4	5.5	10.5	0	2_{II}	2.4	5.5	12.9	0.09
3_{I}	2.4	6.5	11.4	0.83	3_{II}	2.4	6.5	14.0	0.23
4_{I}	2.4	7.5	12.3	1.48	4_{II}	2.4	7.5	15.0	3.02
5_{I}	2.4	8.5	13.1	3.64	5_{II}	2.4	8.5	15.9	5.92
6_{I}	2.4	9.5	13.9	9.01	6_{II}	2.4	9.5	16.8	9.47
7_{I}	2.6	4.5	9.5	0	7_{II}	2.6	4.5	11.6	0
8_{I}	2.6	5.5	10.5	0.01	8_{II}	2.6	5.5	12.9	0.08
9_{I}	2.6	6.5	11.4	1.13	9_{II}	2.6	6.5	14.0	0.25
10_{I}	2.6	7.5	12.3	2.12	10_{II}	2.6	7.5	15.0	3.66
11_{I}	2.6	8.5	13.1	5.03	11_{II}	2.6	8.5	15.9	6.92
12_{I}	2.6	9.5	13.9	12.5	12_{II}	2.6	9.5	16.8	11.8
13_{I}	2.8	4.5	9.5	0	13_{II}	2.8	4.5	11.6	0
14_{I}	2.8	5.5	10.5	0.06	14_{II}	2.8	5.5	12.9	0.14
15_{I}	2.8	6.5	11.4	1.57	15_{II}	2.8	6.5	14.0	0.38
16_{I}	2.8	7.5	12.3	2.73	16_{II}	2.8	7.5	15.0	4.52
17_{I}	2.8	8.5	13.1	6.63	17_{II}	2.8	8.5	15.9	7.88
18_{I}	2.8	9.5	13.9	16	18_{II}	2.8	9.5	16.8	13.4

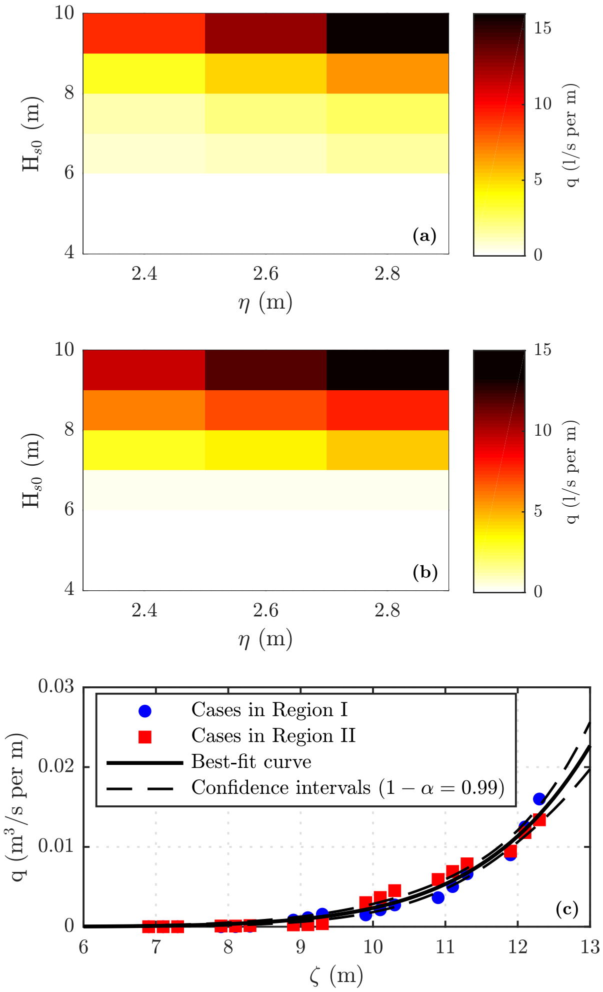

Figure 12: Mean overtopping discharges modelled for wave steepness Regions I (a) and II (b). (c) Mean overtopping discharge (q) variation as a function of the effective overtopping forcing (ζ).

Table 3: Averages of the mean overtopping discharges for constant values of water level and significant wave height in deep water [η: water level; H_{s0}: significant wave height in deep water; $\bar{Q}_{nI}$: average of the mean overtopping discharge in Region I; $\bar{Q}_{nII}$: average of the mean overtopping discharge in Region II].

	$\bar{Q}_{nI}$ ($\mathrm{ls^{-1}m^{-1}}$)	$\bar{Q}_{nII}$ ($\mathrm{ls^{-1}m^{-1}}$)
$\eta = 2.4$ m	2.49	3.12
$\eta = 2.6$ m	3.47	3.79
$\eta = 2.8$ m	4.5	4.39
$H_{s0} = 4.5$ m	0	0
$H_{s0} = 5.5$ m	0.02	0.1
$H_{s0} = 6.5$ m	1.18	0.29
$H_{s0} = 7.5$ m	2.11	3.73
$H_{s0} = 8.5$ m	5.1	6.91
$H_{s0} = 8.5$ m	12.5	11.56

Having established that the mean overtopping rate is mainly driven by water level and significant wave height, for the purposes of this work, we define an *ad hoc* variable, the *effective overtopping forcing*, as

$$\zeta = \eta + H_{s0}. \tag{6}$$

The interest of this new variable is its capacity to predict the overtopping discharge for both regions (I and II). The best-fit curve is:

$$q = k\zeta^9. \tag{7}$$

with $q =$ mean overtopping discharge ($\mathrm{m^2s^{-1}}$) and $k = 2.21\times10^{-12}$ ($\mathrm{m^{-7}s^{-1}}$). The coefficient of determination obtained with Eq. (7) is equal to 0.98, that is, 98% of the variability of the overtopping discharge is explained by Eq. 7. This strong correlation between the *effective overtopping forcing* and the overtopping discharge is also observed in Fig. 12c.

3.6. Operational conditions

The EurOtop [66] indicates that the threshold of overtopping discharge that limits the operational conditions on seawalls protecting a railway is overtopping discharge equal to 5 l/s per m; whereas in the case of seawalls protecting people, this limit is equal to 0.3 l/s per m. As can be observed in Table 2, eleven (twenty-two) of the thirty-six cases exceed the railway (people) threshold.

To better illustrate the operational conditions, Fig. 13 shows the warning level of each (η, H_{s0}) combination for both railway infrastructures and people along with different return period curves. It is observed that a certain value of mean overtopping discharge may have infinite return periods, as it can be the result of infinite (η, H_{s0}) combinations. The separation lines between the different warning levels in Fig. 13 are the isolines of the mean overtopping discharges corresponding to their specific thresholds.

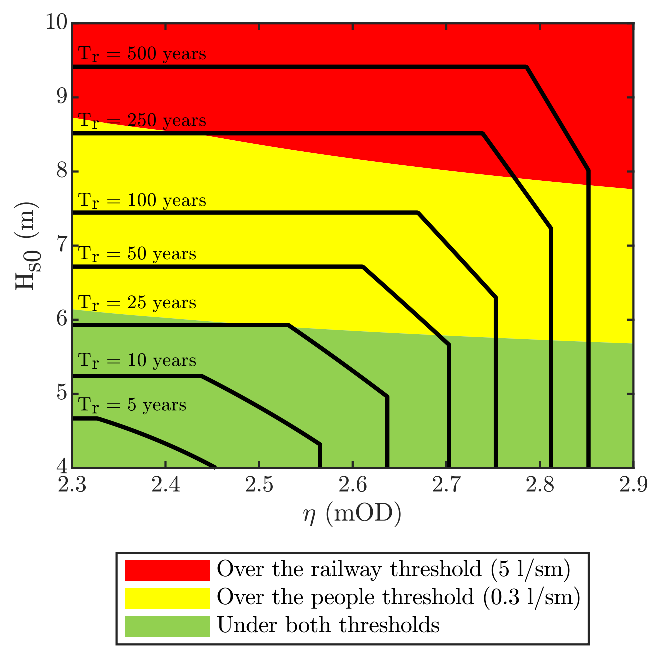

Figure 13: Operational conditions for both the railway and people at the Dawlish seawall. The isolines corresponding to return period values of 5, 10, 25, 50, 100, 250 and 500 years are indicated.

Based on the pairs (η, H_{s0}) included in the isolines of the thresholds, we can assess return periods associated to the different thresholds. The minimum return period associated to the railway threshold is 163.5 years; whereas in the case of people, this return period is 21.8 years. These results show that, according to the thresholds specified by [66], combinations of wave and water level events that could endanger the railway line located in the lee of the Dawlish seawall are expected to occur, on average, every 163 years; whereas the people (e.g., the maintenance workers of the railway lines) would be at risk, on average, every 22 years.

4. Conclusions

In this work, a novel methodology to assess the operational conditions of coastal infrastructures against flooding events is proposed. The methodology was applied to a study case in the UK: the seawall in Dawlish, which is subjected to recurrent overtopping and collapsed under the storm of February 2014. For that, the joint probability of wave and water level data was analysed, and two numerical models (SWAN and OpenFOAM®) were used to propagate waves and compute overtopping discharges for thirty-six different combinations of water level, significant wave height, and spectral peak period. These models were validated through comparisons with wave buoy data and measurements collected during laboratory experiments.

The results show that overtopping rates increase with both significant wave height and water level. Among the thirty-six combinations tested, twenty-nine generated non-zero wave overtopping discharges, twenty-two exceeded the operational limit proposed by the EurOtop for seawalls protecting people (0.3 l/s per m) and eleven were greater than the EurOtop operational threshold for railway lines in the lee of coastal structures (5 l/s per m). The maximum wave overtopping discharge obtained was 16 l/s per m. To characterise the joint action of the two main variables that drive wave overtopping (significant wave height and water level), we defined a new variable: the *effective overtopping forcing*, which was proven to explain 98% of the variability of the overtopping discharge.

The methodology was also applied to obtain the return periods associated to the thresholds that limit the operational conditions for railway and people uses. It was obtained that the minimum return period associated to the railway (people) threshold is 163.5 years (21.8 years). Apart from these two specific applications, the developed methodology could be used to compute the return period associated with any other overtopping discharge value. In addition, it could be applied to calculate the overtopping discharge induced by any sea state. Thus, we can check if a certain coastal infrastructure is going to be operational under any expected marine condition.

The composite methodology presented and applied in this work, which comprises advanced statistical techniques involving, laboratory experiments and two different types of numerical models, is also extensible to other coastal regions across the globe. It represents an advanced tool to assess the operational conditions for different uses as well as to analyse the possible consequences of flooding events on transport infrastructures and urban developments located in the lee of coastal structures.

Acknowledgements

This work was carried out in the framework of the WAVEIMPACT Marie Curie fellowship (PCIG-13-GA-2013-618556, European Commission, Marie Curie fellowship, fellow GI) and the ICE project (Intelligent Community Energy, European Commision, Contract no. 5025). CRD and RB were partly funded by the University of Plymouth and the Spanish Ministry of Science, Innovation and Universities (*Programa Juan de la Cierva 2017*, FJCI-2017-31781), respectively.

References

[1] A. Sperotto, S. Torresan, V. Gallina, E. Coppola, A. Critto, A. Marcomini, A multi-disciplinary approach to evaluate pluvial floods risk under changing climate: The case study of the municipality of Venice (Italy), Science of the Total Environment 562 (2016) 1031–1043.

[2] S. Xian, J. Yin, N. Lin, M. Oppenheimer, Influence of risk factors and past events on flood resilience in coastal megacities: Comparative analysis of NYC and Shanghai, Science of the Total Environment 610 (2018) 1251–1261.

[3] R. J. Bergillos, C. Rodriguez-Delgado, J. Allen, G. Iglesias, Wave energy converter geometry for coastal flooding mitigation, Science of the Total Environment 668 (2019) 1232–1241.

[4] J. Fang, D. Lincke, S. Brown, R. J. Nicholls, C. Wolff, J.-L. Merkens, J. Hinkel, A. T. Vafeidis, P. Shi, M. Liu, Coastal flood risks in China through the 21st century–An application of DIVA, Science of the Total Environment (2019) 135311.

[5] A. G. Rumson, S. H. Hallett, Innovations in the use of data facilitating insurance as a resilience mechanism for coastal flood risk, Science of the Total Environment 661 (2019) 598–612.

[6] L. Vamvakeridou-Lyroudia, A. Chen, M. Khoury, M. Gibson, A. Kostaridis, D. Stewart, M. Wood, S. Djordjevic, D. Savic, Assessing and visualising hazard impacts to enhance the resilience of critical infrastructures to urban flooding, Science of The Total Environment 707 (2020) 136078.

[7] T. Gallien, B. Sanders, R. Flick, Urban coastal flood prediction: Integrating wave overtopping, flood defenses and drainage, Coastal Engineering 91 (2014) 18–28.

[8] T. Gallien, Validated coastal flood modeling at Imperial Beach, California: Comparing total water level, empirical and numerical overtopping methodologies, Coastal Engineering 111 (2016) 95–104.

[9] D. Xie, Q.-P. Zou, A. Mignone, J. D. MacRae, Coastal flooding from wave overtopping and sea level rise adaptation in the northeastern USA, Coastal Engineering 150 (2019) 39–58.

[10] G. Iglesias, J. Abanades, Wave power - climate change mitigation and adaptation, in: L. M. Chen W.-Y., Suzuki T. (Ed.), Handbook of Climate Change Mitigation and Adaptation. Springer New York, p. 1-49, 2015.

[11] S. Muis, B. Güneralp, B. Jongman, J. C. Aerts, P. J. Ward, Flood risk and adaptation strategies under climate change and urban expansion: A probabilistic analysis using global data, Science of the Total Environment 538 (2015) 445–457.

[12] A. Sánchez-Arcilla, M. García-León, V. Gracia, R. Devoy, A. Stanica, J. Gault, Managing coastal environments under climate change: Pathways to adaptation, Science of the Total Environment 572 (2016) 1336–1352.

[13] J. Wang, S. Yi, M. Li, L. Wang, C. Song, Effects of sea level rise, land subsidence, bathymetric change and typhoon tracks on storm flooding in the coastal areas of Shanghai, Science of the Total Environment 621 (2018) 228–234.

[14] R. J. Bergillos, C. Rodriguez-Delgado, G. Iglesias, Wave farm impacts on coastal flooding under sea-level rise: a case study in southern Spain, Science of the Total Environment 653 (2019) 1522–1531.

[15] G. Bove, A. Becker, B. Sweeney, M. Vousdoukas, S. Kulp, A method for regional estimation of climate change exposure of coastal infrastructure: Case of USVI and the influence of digital elevation models on assessments, Science of The Total Environment 710 (2020) 136162.

[16] A. Bomers, J. P. Aguilar Lopez, J. J. Warmink, S. J. M. H. Hulscher, Modelling effects of an asphalt road at a dike crest on dike cover erosion onset during wave overtopping, Natural Hazards (2018).

[17] T. Thieu Quang, H. Oumeraci, Numerical modelling of wave overtopping-induced erosion of grassed inner sea-dike slopes, Natural Hazards 63 (2012) 417–447.

[18] J.-L. de Kok, M. Grossmann, Large-scale assessment of flood risk and the effects of mitigation measures along the elbe river, Natural Hazards 52 (2010) 143–166.

[19] H. T. Le, H. J. Verhagen, J. K. Vrijling, Damage to grass dikes due to wave overtopping, Natural Hazards 86 (2017) 849–875.

[20] F. Chiganne, C. Marche, T.-F. Mahdi, Evaluation of the overflow failure scenario and hydrograph of an embankment dam with a concrete upstream slope protection, Natural Hazards 71 (2014) 21–39.

[21] S.-J. Wu, J.-C. Yang, Y.-K. Tung, Risk analysis for flood-control structure under consideration of uncertainties in design flood, Natural Hazards 58 (2011) 117–140.

[22] A. Y. Hoekstra, J.-L. De Kok, Adapting to climate change: a comparison of two strategies for dike heightening, Natural Hazards 47 (2008) 217–228.

[23] Q. Zhong, W. Wu, S. Chen, M. Wang, Comparison of simplified physically based dam breach models, Natural Hazards 84 (2016) 1385–1418.

[24] N. Javadi, T.-F. Mahdi, Experimental investigation into rockfill dam failure initiation by overtopping, Natural Hazards 74 (2014) 623–637.

[25] D. Vicinanza, I. Cáceres, M. Buccino, X. Gironella, M. Calabrese, Wave disturbance behind low-crested structures: Diffraction and overtopping effects, Coastal Engineering 56 (2009) 1173–1185.

[26] C. Iuppa, L. Cavallaro, R. E. Musumeci, D. Vicinanza, E. Foti, Empirical overtopping volume statistics at an OBREC, Coastal Engineering 152 (2019) 103524.

[27] A. J. Evans, B. Garrod, L. B. Firth, S. J. Hawkins, E. S. Morris-Webb, H. Goudge, P. J. Moore, Stakeholder priorities for multi-functional coastal defence developments and steps to effective implementation, Marine Policy 75 (2017) 143 – 155.

[28] Q. Yu, A. K. H. Lau, K. T. Tsang, J. C. H. Fung, Human damage assessments of coastal flooding for hong kong and the pearl river delta due to climate change-related sea level rise in the twenty-first century, Natural Hazards 92 (2018) 1011–1038.

[29] S. F. Silva, M. Martinho, R. Capito, T. Reis, C. J. Fortes, J. C. Ferreira, An index-based method for coastal-flood risk assessment in low-lying areas (costa de caparica, portugal), Ocean & Coastal Management 144 (2017) 90 – 104.

[30] Y. Fang, J. Yin, B. Wu, Flooding risk assessment of coastal tourist attractions affected by sea level rise and storm surge: a case study in zhejiang province, china, Natural Hazards 84 (2016) 611–624.

[31] T. Gallien, W. O'Reilly, R. Flick, R. Guza, Geometric properties of anthropogenic flood control berms on southern California beaches, Ocean & Coastal Management 105 (2015) 35 – 47.

[32] P. Bernatchez, C. Fraser, D. Lefaivre, S. Dugas, Integrating anthropogenic factors, geomorphological indicators and local knowledge in the analysis of coastal flooding and erosion hazards, Ocean & Coastal Management 54 (2011) 621 – 632.

[33] M. P. Bunicontro, S. C. Marcomini, R. A. López, The effect of coastal defense structures (mounds) on southeast coast of Buenos Aires province, Argentine, Ocean & Coastal Management 116 (2015) 404 – 413.

[34] A. Carrasco, Ó. Ferreira, A. Matias, P. Freire, Flood hazard assessment and management of fetch-limited coastal environments, Ocean & Coastal Management 65 (2012) 15 – 25.

[35] N. P. Kurian, N. Nirupama, M. Baba, K. V. Thomas, Coastal flooding due to synoptic scale, meso-scale and remote forcings, Natural Hazards 48 (2009) 259–273.

[36] I.-J. Moon, I. S. Oh, T. Murty, Y.-H. Youn, Causes of the unusual coastal flooding generated by typhoon winnie on the west coast of korea, Natural Hazards 29 (2003) 485–500.

[37] J. Geeraerts, P. Troch, J. De Rouck, H. Verhaeghe, J. J. Bouma, Wave overtopping at coastal structures: prediction tools and related hazard analysis, Journal of Cleaner Production 15 (2007) 1514–1521.

[38] H. Schüttrumpf, H. Oumeraci, Layer thicknesses and velocities of wave overtopping flow at seadikes, Coastal Engineering 52 (2005) 473 – 495.

[39] T. Suzuki, C. Altomare, W. Veale, T. Verwaest, K. Trouw, P. Troch, M. Zijlema, Efficient and robust wave overtopping estimation for impermeable coastal structures in shallow foreshores using SWASH, Coastal Engineering 122 (2017) 108 – 123.

[40] C. Coelho, T. Cruz, P. Roebeling, Longitudinal revetments to mitigate overtopping and flooding: Effectiveness, costs and benefits, Ocean & Coastal Management 134 (2016) 93 – 102.

[41] B. Renard, M. Lang, Use of a Gaussian copula for multivariate extreme value analysis: Some case studies in hydrology, Advances in Water Resources 30 (2007) 897 – 912.

[42] J. A. Tawn, Bivariate extreme value theory: Models and estimation, Biometrika 75 (1988) 397–415.

[43] I. Morton, J. Bowers, Extreme value analysis in a multivariate offshore environment, Applied Ocean Research 18 (1996) 303 – 317.

[44] M. Kramer, B. Zanuttigh, J. Van der Meer, C. Vidal, F. Gironella, Laboratory experiments on low-crested breakwaters, Coastal Engineering 52 (2005) 867–885.

[45] S. A. Hughes, N. Nadal, Laboratory study of combined wave overtopping and storm surge overflow of a levee, Coastal Engineering 56 (2009) 244–259.

[46] T. Pullen, W. Allsop, T. Bruce, J. Pearson, Field and laboratory measurements of mean overtopping discharges and spatial distributions at vertical seawalls, Coastal Engineering 56 (2009) 121–140.

[47] J. W. van der Meer, H. Verhaeghe, G. J. Steendam, The new wave overtopping database for coastal structures, Coastal Engineering 56 (2009) 108 – 120. The CLASH Project.

[48] D. Gallach-Sánchez, P. Troch, T. Vroman, L. Pintelon, A. Kortenhaus, Experimental study of overtopping performance of steep smooth slopes for shallow water wave conditions, in: Proceedings of the 5th Conference on the Application of Physical Modelling to Port and Coastal Protection (Coastlab14). Varna, Bulgaria, 2014.

[49] Y. Pan, C. Kuang, L. Li, F. Amini, Full-scale laboratory study on distribution of individual wave overtopping volumes over a levee under negative freeboard, Coastal Engineering 97 (2015) 11–20.

[50] C. Iuppa, P. Contestabile, L. Cavallaro, E. Foti, D. Vicinanza, Hydraulic performance of an innovative breakwater for overtopping wave energy conversion, Sustainability 8 (2016) 1226.

[51] M. Salauddin, J. Pearson, Laboratory investigation of overtopping at a sloping structure with permeable shingle foreshore, Ocean Engineering 197 (2020) 106866.

[52] X. Chen, B. Hofland, C. Altomare, T. Suzuki, W. Uijttewaal, Forces on a vertical wall on a dike crest due to overtopping flow, Coastal Engineering 95 (2015) 94 – 104.

[53] K. Pillai, A. Etemad-Shahidi, C. Lemckert, Wave overtopping at berm breakwaters: Experimental study and development of prediction formula, Coastal Engineering 130 (2017) 85–102.

[54] K. V. Doorslaer, A. Romano, J. D. Rouck, A. Kortenhaus, Impacts on a storm wall caused by non-breaking waves overtopping a smooth dike slope, Coastal Engineering 120 (2017) 93 – 111.

[55] J. Molines, J. R. Medina, Calibration of overtopping roughness factors for concrete armor units in non-breaking conditions using the CLASH database, Coastal Engineering 96 (2015) 62 – 70.

[56] B. Zanuttigh, S. M. Formentin, J. W. van der Meer, Prediction of extreme and tolerable wave overtopping discharges through an advanced neural network, Ocean Engineering 127 (2016) 7–22.

[57] J. Molines, M. P. Herrera, J. R. Medina, Estimations of wave forces on crown walls based on wave overtopping rates, Coastal Engineering 132 (2018) 50 – 62.

[58] J. Molines, M. P. Herrera, M. E. Gómez-Martín, J. R. Medina, Distribution of individual wave overtopping volumes on mound breakwaters, Coastal Engineering 149 (2019) 15–27.

[59] C. Altomare, T. Suzuki, X. Chen, T. Verwaest, A. Kortenhaus, Wave overtopping of sea dikes with very shallow foreshores, Coastal Engineering 116 (2016) 236 – 257.

[60] N. Kobayashi, A. Farhadzadeh, J. Melby, B. Johnson, M. Gravens, Wave overtopping of levees and overwash of dunes, Journal of Coastal Research (2010) 888–900.

[61] K. Hu, C. Mingham, D. Causon, Numerical simulation of wave overtopping of coastal structures using the non-linear shallow water equations, Coastal Engineering 41 (2000) 433 – 465.

[62] S. Shao, C. Ji, D. I. Graham, D. E. Reeve, P. W. James, A. J. Chadwick, Simulation of wave overtopping by an incompressible SPH model, Coastal Engineering 53 (2006) 723 – 735.

[63] M. J. Wesley, K. F. Cheung, Modeling of wave overtopping on vertical structures with the HLLS Riemann solver, Coastal Engineering 112 (2016) 28 – 43.

[64] C. Hirt, B. Nichols, Volume of fluid (VOF) method for the dynamics of free boundaries, Journal of Computational Physics 39 (1981) 201 – 225.

[65] L. Franco, M. de Gerloni, J. van der Meer, Wave overtopping at vertical and composite breakwaters, Proc. 24th ICCE, Kobe, October 23-28, 1994 (1994).

[66] J. Van der Meer, N. Allsop, T. Bruce, J. De Rouck, A. Kortenhaus, T. Pullen, H. Schüttrumpf, P. Troch, B. Zanuttigh, EurOtop, Manual on wave overtopping of sea defences and related structures. An overtopping manual largely based on European research, but for worldwide application, Technical Report, 2018.

[67] T. Petroliagkis, E. Voukouvalas, J. Disperati, J. Bidlot, Joint probabilities of storm surge, significant wave height and river discharge components of coastal flooding events, European Commission-JRC Technical Reports (2016).

[68] L. Holthuijsen, N. Booij, R. Ris, A spectral wave model for the coastal zone, ASCE, 1993.

[69] N. Booij, R. C. Ris, L. H. Holthuijsen, A third-generation wave model for coastal regions: 1. Model description and validation, Journal of Geophysical Research: Oceans 104 (1999) 7649–7666.

[70] R. J. Bergillos, A. López-Ruiz, M. Ortega-Sánchez, G. Masselink, M. A. Losada, Implications of delta retreat on wave propagation and longshore sediment transport-Guadalfeo case study (southern Spain), Marine Geology 382 (2016) 1–16.

[71] R. J. Bergillos, G. Masselink, R. T. McCall, M. Ortega-Sánchez, Modelling overwash vulnerability along mixed sand-gravel coasts with XBeach-G: Case study of Playa Granada, southern Spain, in: Coastal Engineering Proceedings, volume 1 (35), 2016, p. 13.

[72] A. López-Ruiz, R. J. Bergillos, M. Ortega-Sánchez, The importance of wave climate forecasting on the decision-making process for nearshore wave energy exploitation, Applied energy 182 (2016) 191–203.

[73] A. López-Ruiz, R. J. Bergillos, M. Ortega-Sánchez, M. A. Losada, Impact of river regulation on the submerged morphology of a Mediterranean deltaic system: evaluating Coastal Engineering tools, in: Coastal Engineering Proceedings, volume 1 (35), 2016, p. 10.

[74] R. J. Bergillos, C. Rodríguez-Delgado, M. Ortega-Sánchez, Advances in management tools for modeling artificial nourishments in mixed beaches, Journal of Marine Systems 172 (2017) 1–13.

[75] R. J. Bergillos, G. Masselink, M. Ortega-Sánchez, Coupling cross-shore and longshore sediment transport to model storm response along a mixed sand-gravel coast under varying wave directions, Coastal Engineering 129 (2017) 93–104.

[76] R. J. Bergillos, A. López-Ruiz, D. Principal-Gómez, M. Ortega-Sánchez, An integrated methodology to forecast the efficiency of nourishment strategies in eroding deltas, Science of the Total Environment 613 (2018) 1175–1184.

[77] R. J. Bergillos, A. Lopez-Ruiz, E. Medina-Lopez, A. Monino, M. Ortega-Sanchez, The role of wave energy converter farms on coastal protection in

eroding deltas, Guadalfeo, southern Spain, Journal of Cleaner Production 171 (2018) 356–367.

[78] A. López-Ruiz, R. J. Bergillos, J. M. Raffo-Caballero, M. Ortega-Sánchez, Towards an optimum design of wave energy converter arrays through an integrated approach of life cycle performance and operational capacity, Applied Energy 209 (2018) 20–32.

[79] A. López-Ruiz, R. J. Bergillos, A. Lira-Loarca, M. Ortega-Sánchez, A methodology for the long-term simulation and uncertainty analysis of the operational lifetime performance of wave energy converter arrays, Energy 153 (2018) 126–135.

[80] P. Magaña, R. J. Bergillos, J. Del-Rosal-Salido, M. A. Reyes-Merlo, P. Díaz-Carrasco, M. Ortega-Sánchez, Integrating complex numerical approaches into a user-friendly application for the management of coastal environments, Science of the Total Environment 624 (2018) 979–990.

[81] C. Rodriguez-Delgado, R. J. Bergillos, M. Ortega-Sánchez, G. Iglesias, Protection of gravel-dominated coasts through wave farms: Layout and shoreline evolution, Science of The Total Environment 636 (2018) 1541–1552.

[82] C. Rodriguez-Delgado, R. J. Bergillos, M. Ortega-Sánchez, G. Iglesias, Wave farm effects on the coast: The alongshore position, Science of the Total Environment 640 (2018) 1176–1186.

[83] C. Rodriguez-Delgado, R. J. Bergillos, G. Iglesias, Dual wave energy converter farms and coastline dynamics: the role of inter-device spacing, Science of the Total Environment 646 (2019) 1241–1252.

[84] R. J. Bergillos, C. Rodriguez-Delgado, J. Allen, G. Iglesias, Wave energy converter configuration in dual wave farms, Ocean Engineering 178 (2019) 204–214.

[85] C. Rodriguez-Delgado, R. J. Bergillos, G. Iglesias, Dual wave farms for energy production and coastal protection under sea level rise, Journal of Cleaner Production 222 (2019) 364–372.

[86] C. Rodriguez-Delgado, R. J. Bergillos, G. Iglesias, An artificial neural network model of coastal erosion mitigation through wave farms, Environmental Modelling and Software 119 (2019) 390–399.

[87] H. G. Weller, G. Tabor, H. Jasak, C. Fureby, A tensorial approach to computational continuum mechanics using object-oriented techniques, Computers in Physics 12 (1998) 620–631.

[88] D. Dawson, J. Shaw, W. R. Gehrels, Sea-level rise impacts on transport infrastructure: The notorious case of the coastal railway line at Dawlish, England, Journal of Transport Geography 51 (2016) 97 – 109.

[89] C. G. Soares, M. Scotto, Application of the r largest-order statistics for long-term predictions of significant wave height, Coastal Engineering 51 (2004) 387 – 394.